

Finite Element Analysis of Particle Assembly-water Coupled Frictional Contact Problem

S. Ozaki¹, K. Hashiguchi², T. Okayasu² and D.H. Chen¹

Abstract: In order to analyze precisely not only the elastoplastic deformation phenomenon of saturated particle assembly such as soils, grains, powdered and tablet medicines or three dimensional cellular materials, but also the frictional sliding phenomenon between saturated particle assembly and other bodies, a particle assembly-water coupled finite element program, that incorporates both the *subloading surface* and the *subloading-friction models*, is developed. Subsequently, simulations of the compaction behavior of saturated particle assembly under strain rate control are performed. It is revealed by the numerical experiment adopting the finite element program that the frictional sliding behavior of the contact boundary influences both the deformation behavior and the pore water flow behavior in the saturated particle assembly.

Keyword: Frictional contact, particle assembly-water coupled problem, FEM, subloading surface, unconventional elastoplasticity, compaction phenomenon.

1 Introduction

For the analysis of the deformation of saturated particle assembly, we would have to consider the following mechanical phenomena.

- 1) The deformation of the particle assembly saturated by the pore water must be analyzed as the coupled phenomenon of the deformation of the skeleton of particle assembly and the flow of the pore water [e.g., Cristian, 1968; Cristian and Boehrner, 1970; Akai and Tamura,

1978; Asaoka et al., 1994, 1995, 1997; Asaoka et al., 1998; Asaoka et al., 2000; Ferguson and Palanathakumar, 2005; Liu and Scarpas, 2005].

- 2) Particle assembly exposed to atmospheric pressure on the free surface is in a heavily over-consolidated state and thus exhibits softening behavior. Besides, they are frequently subjected to the cyclic loading due to earthquake and vibration treatment, etc. Therefore, an elastoplastic constitutive equation capable of appropriately describing the softening and cyclic behavior has to be incorporated. It has to fall within the framework of unconventional elastoplasticity [Drucker, 1988], which excludes the postulate that the interior of a yield surface is an elastic domain, and thus it is capable of describing the plastic strain rate due to the rate of stress inside the yield surface. Among various unconventional elastoplastic constitutive models, the *subloading surface model* [Hashiguchi, 1978, 1980, 1989] has a high rationality fulfilling the *continuity* and *smoothness conditions* [Hashiguchi, 1993a, b, 1994, 2000]. Further, it possesses the controlling function for the stress to approach the yield surface in the plastic loading process and thus it is not required to incorporate an operation pulling back the stress to the yield surface such as the return-mapping, mean-normal methods in numerical analyses. The subloading surface model has been widely applied to the prediction of the deformation behavior of metals and soils.
- 3) A rational treatment for the contact boundaries between analyzed bodies is required, while friction force and/or sliding are induced in almost all engineering problems. Moreover, it

¹ Tokyo University of Science, Kudankita 1-14-6, Chiyoda-ku, Tokyo, Japan.

² Kyushu University, Hakozaki 6-10-1, Higashi-ku, Fukuoka, Japan.

is observed in experiments that the tangential traction (contact stress) gradually increases with the relative displacement between contact bodies [e.g., Courtney-Pratt and Eisner, 1957; Desai et al., 1985; Uesugi and Kishida, 1986; Olofsson, 1995; Olofsson and Hagman, 1997; Hagman and Olofsson, 1998]. This phenomenon cannot be described by the conventional friction model [e.g., Curnier, 1984; Cheng and Kikuchi, 1985; Kikuchi and Oden, 1988; Wriggers et al., 1990; Peric and Owen, 1992; Wriggers, 2003], including the classical Coulomb friction model. In the conventional friction models, the variation of traction inside the *sliding-yield surface* (frictional criterion) does not induce sliding displacement. Needless to say, the accumulation of sliding displacement by the cyclic loading of traction inside the sliding-yield surface cannot be predicted. In order to overcome these defects in the conventional friction model, an unconventional friction model, called *the subloading-friction model* [Hashiguchi et al., 2005], has been proposed based on the concept of the subloading surface, which enables us to describe the sliding velocity due to the rate of traction inside the sliding-yield surface.

In this study, particle assembly-water coupled finite element programming is implemented by incorporating the subloading surface model and the subloading-friction model. The program is then applied to the analysis of the compaction behavior of the saturated particle assembly subjected to a constant strain rate under drainage condition in order to reveal the influence of frictional property in the contact surface with the steel ring. Then, it is verified that the frictional sliding behavior of the contact boundary as well as the pore water flow influences the deformation behavior of saturated particle assembly.

2 Finite element implementation for particle assembly-water coupled contact problem

The finite element implementation for the particle assembly-water coupled problem based on the *principle of effective stress* is explained below.

Further, the penalty method and the Lagrange multiplier method are adopted for treatments of the frictional contact and particle assembly-water coupling, respectively, while these methods are useful and easy to incorporate constrained conditions into the finite element program. Here, the analysis is limited to the infinitesimal deformation and it is assumed that the spin of material is negligible and thus only the material-time derivative of stress ($\dot{\cdot}$) is adopted for simplicity.

2.1 Governing equations

The rate form of the equilibrium equation is given by

$$\int_V (\text{div} \dot{\boldsymbol{\sigma}}^T + \rho_w (\text{tr} \mathbf{D}) \mathbf{b}) dV = \mathbf{0}, \quad (1)$$

where $\boldsymbol{\sigma}$ is the true (Cauchy) stress; \mathbf{D} the strain rate; \mathbf{b} the body force vector; and ρ_w the mass density of the pore water. The symbols $\text{div}(\cdot)$, $\text{tr}(\cdot)$, $(\cdot)^T$ and $\int_V dV$ denote the divergence, trace, transpose and volume-integration, respectively. On the other hand, the equations of continuity for the particle assembly and the pore water are given as follows:

$$\mathbf{L} = \partial \mathbf{v} / \partial \mathbf{x}, \quad \mathbf{D} = (\mathbf{L} + \mathbf{L}^T) / 2, \quad (2)$$

$$\left(\int_V dV \right) \dot{\cdot} = \int_V \text{tr} \mathbf{D} dV = - \int_S \mathbf{v}_w \cdot \bar{\mathbf{n}} dS, \quad (3)$$

where \mathbf{L} is the velocity gradient; \mathbf{v} the velocity of material point \mathbf{x} ; \mathbf{v}_w the discharge velocity of pore water; and $\bar{\mathbf{n}}$ the unit outward-normal vector on the objective body. $\int_S dS$ denotes the integration over the surface.

The state of contact between the two bodies is shown in Fig. 1. The equilibrium between the contact traction \mathbf{f} acting on the analyzed body and the contact traction \mathbf{F} acting on the external body is given by

$$\mathbf{F} = -\mathbf{f}. \quad (4)$$

Based on the principle of effective stress, the effective stress $\boldsymbol{\sigma}'$ and the effective contact traction \mathbf{f}' are given as follows:

$$\boldsymbol{\sigma} = \boldsymbol{\sigma}' - p_w \mathbf{I}, \quad (5)$$

$$\mathbf{f} = \mathbf{f}' - p_w \mathbf{n}, \quad (6)$$

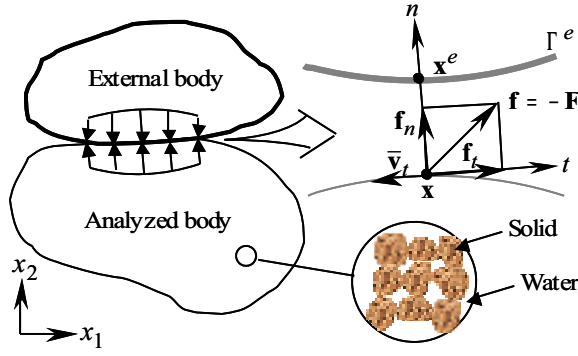


Figure 1: Two bodies in contact

where p_w , \mathbf{I} and \mathbf{n} are the pore water pressure (positive for compression), the identity tensor, and the unit outward-normal vector on the analyzed body, respectively. In this study, we assume that there is no frictional resistance between the particle assembly and the pore water.

From Eqs. (4)-(6), the generalized equilibrium of the contact traction can be described as

$$\mathbf{F}' - BP_w \mathbf{n}^e = -(\mathbf{f}' - \beta p_w \mathbf{n}), \quad (7)$$

where P_w and \mathbf{n}^e are the pore water pressure and the unit outward-normal vector of the external body, respectively. It should be noted that B ($0 \leq B \leq 1$) and β ($0 \leq \beta \leq 1$) are the parameters that denote the permeability of the external and analyzed bodies, respectively. For instance, assuming the rigid plate (e.g., metal and concrete) and the saturated particle assembly to be the external body and the analyzed body, respectively, Eq. (7) can be rewritten as

$$\mathbf{F} = \mathbf{F}' = -(\mathbf{f}' - p_w \mathbf{n}) \quad \text{for } B = 0 \text{ and } \beta = 1. \quad (8)$$

On the other hand, if we assume that the external body has a high permeability as seen in porous stones or cellular solids, Eq.(7) can be rewritten as

$$\mathbf{F}' - P_w \mathbf{N} = -(\mathbf{f}' - p_w \mathbf{n}) \quad \text{for } B = 1 \text{ and } \beta = 1. \quad (9)$$

In the following analysis, we investigate the mechanical behavior induced in the compaction test of saturated soil under the condition given in Eq. (8) for the contact boundary (periphery of saturated particle assembly).

2.2 Boundary conditions

We adopt the boundary condition based on the *master-slave concept* for the frictional contact [e.g., Curnier, 1984; Cheng and Kikuchi, 1985; Wriggers et al., 1990; Peric and Owen, 1992; Wriggers, 2003] in the formulation of the boundary value problem. Here, the master body implies the external one and the slave body the analyzed one.

Let the boundary surfaces of bodies be denoted by Γ , which consist of the traction rate boundary Γ_t , the displacement rate boundary Γ_v , the contact boundary Γ_c , the total water head boundary Γ_h , and the flux boundary Γ_q as shown in Fig. 2. Here, the superscripts (e) and (a) denote the boundaries of the external (master) and analyzed (slave) bodies, respectively. Since, in general, Γ_c varies during the deformation, the variation should always be judged by using the contact condition mentioned below.

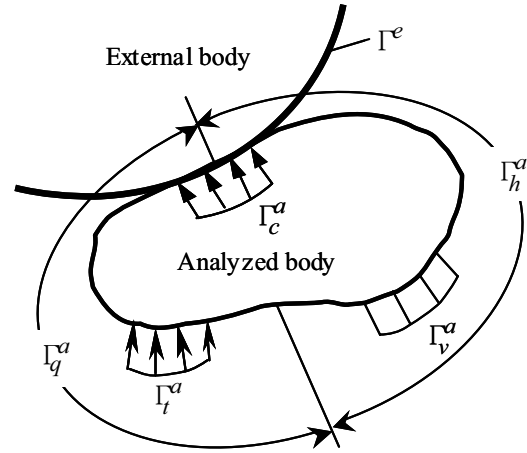


Figure 2: Boundary condition of particle assembly-water coupled contact problems

The gap (i.e. the minimum distance g_n from the boundary surface of the analyzed body to the surface of the external body) should be zero, and the normal component of the total traction vector f_n applied to the analyzed body should become positive when the two bodies come into contact. Thus, the contact condition is given by

$$g_n \geq 0, \quad f_n \geq 0, \quad f_n g_n = 0 \quad (10)$$

or

$$g_n \geq 0, \quad f'_n - p_{wn} \geq 0, \quad (f'_n - p_{wn})g_n = 0, \quad (11)$$

where

$$g_n \equiv (\mathbf{x}^e - \mathbf{x}) \cdot \mathbf{n}, \quad f_n = \mathbf{f} \cdot \mathbf{n}, \quad p_{wn} = p_w \mathbf{n} \cdot \mathbf{n}, \quad (12)$$

\mathbf{x}^e and \mathbf{x} are the position vectors of the material points on the boundary surfaces of the external body (rigid plate) and analyzed body (particle assembly), respectively.

Therefore, the boundary conditions of the particle assembly-water coupled problem that include the frictional contact of the analyzed body are given by

$$\left. \begin{aligned} \Gamma_c &= \Gamma^a \cap \Gamma^e, \\ \Gamma^a &= \Gamma_v^a \cup \Gamma_t^a \cup \Gamma_c^a = \Gamma_h^a \cup \Gamma_q^a, \\ \Gamma_c &\in \Gamma_h^a \cup \Gamma_q^a, \end{aligned} \right\} \quad (13)$$

$$\left. \begin{aligned} \mathbf{v} &= \underline{\mathbf{v}} && \text{on } \Gamma_v^a, \\ \dot{\boldsymbol{\sigma}} \cdot \mathbf{n} &= \underline{\dot{\mathbf{t}}} && \text{on } \Gamma_t^a, \\ h &= \underline{h} && \text{on } \Gamma_h^a, \\ \mathbf{v}_w &= \underline{\mathbf{v}}_w && \text{on } \Gamma_q^a, \\ \dot{\boldsymbol{\sigma}} \cdot \mathbf{n} &= \mathbf{0} && \text{if } g_n > 0 \text{ and } f_n = 0 \\ \dot{\boldsymbol{\sigma}} \cdot \mathbf{n} &= -\dot{\mathbf{f}} && \text{if } g_n = 0 \text{ and } f_n > 0 \end{aligned} \right\} \text{ on } \Gamma_c^a, \quad (14)$$

where h and $\dot{\mathbf{t}}$ are the total water head and the traction rate, respectively, and $(\underline{\quad})$ denotes the known value.

The relative velocity $\bar{\mathbf{v}}$ at the contact surface is given by

$$\bar{\mathbf{v}} = \mathbf{v}^e - \mathbf{v}, \quad (15)$$

where \mathbf{v} and \mathbf{v}^e are the velocities of the material points \mathbf{x} and \mathbf{x}^e , respectively.

2.3 Constitutive equations

The constitutive equations for deformation and friction are expressed as

$$\dot{\boldsymbol{\sigma}}' = \mathbf{C}^{ep} \mathbf{D}, \quad (16)$$

$$\dot{\mathbf{f}}' = \mathbf{C}^f \bar{\mathbf{v}}, \quad (17)$$

where \mathbf{C}^{ep} and \mathbf{C}^f are the elastoplastic stiffness and the frictional stiffness moduli, respectively, and their explicit forms will be given in the next section.

In this article, we assume that the velocity of pore water obeys the *Darcy's law* described by

$$\mathbf{v}_w = -k \frac{\partial h}{\partial \mathbf{x}} = -k \frac{\partial}{\partial \mathbf{x}} \left(z + \frac{p_w}{\gamma_w} \right), \quad (18)$$

where k , z , and γ_w are the coefficient of permeability, the potential head, and the weight per unit volume of pore water, respectively. Here, the coefficient of permeability is a scalar constant value.

2.4 Principle of virtual work

Let us consider two admissible displacement fields that satisfy the equilibrium and boundary conditions. The difference between the quantities of these fields is denoted by $\delta(\quad)$, which is sometimes also referred to as the *test function*. Thus, Eq. (1) is rewritten as follows:

$$\int_V (\text{div} \dot{\boldsymbol{\sigma}}^T + \rho_w (\text{tr} \mathbf{D}) \mathbf{b}) \cdot \delta \mathbf{v} dV = \mathbf{0}. \quad (19)$$

Applying the Gauss's divergence theorem and the boundary condition (14) into Eq. (19), one has

$$\begin{aligned} \int_V \dot{\boldsymbol{\sigma}}' : \delta \mathbf{D} dV + \int_V \rho_w (\text{tr} \mathbf{D}) \mathbf{b} \cdot \delta \mathbf{v} dV - \int_V \dot{p}_w \mathbf{I} : \delta \mathbf{D} dV \\ = \int_S \dot{\mathbf{t}} \cdot \delta \mathbf{v} dS, \end{aligned} \quad (20)$$

where $(:)$ denotes second-order scalar products.

On the other hand, the virtual work rate with respect to the contact traction is described by Eq. (8) as

$$\begin{aligned} \delta \dot{W}^c &= \int_S \dot{\mathbf{F}} \cdot \delta \mathbf{v}^e dS + \int_S \dot{\mathbf{f}} \cdot \delta \mathbf{v} dS \\ &= \int_S -\dot{\mathbf{f}} \cdot \delta \bar{\mathbf{v}} dS \\ &= - \int_S (\dot{\mathbf{f}}' - \dot{p}_w \mathbf{n}) \cdot \delta \bar{\mathbf{v}} dS, \end{aligned} \quad (21)$$

where

$$\delta \bar{\mathbf{v}} = \delta \mathbf{v}^e - \delta \mathbf{v}. \quad (22)$$

Considering the frictional contact as a constrained condition based on the penalty method, the rate form of the principle of virtual work for the particle assembly-water coupled problem can be obtained from Eqs. (20) and (21) as follows:

$$\begin{aligned} \int_V \dot{\boldsymbol{\sigma}}' : \delta \mathbf{D} dV + \int_V \rho_w (\text{tr} \mathbf{D}) \mathbf{b} \cdot \delta \mathbf{v} dV - \int_V \dot{p}_w \mathbf{I} : \delta \mathbf{D} dV \\ = \int_S \dot{\mathbf{t}} \cdot \delta \mathbf{v} dS - \int_S (\dot{\mathbf{f}}' - \dot{p}_w \mathbf{n}) \cdot \delta \bar{\mathbf{v}} dS, \quad (23) \end{aligned}$$

2.5 Finite element discretization

The volume-integration of Eq. (23) is performed over whole finite elements included in a continuous media. Hereafter, the symbols $\{\}$ and $[\]$ are used below to denote a vector and matrix, respectively. In what follows, we assume the two dimensional coupled contact problem.

The velocity field inside the element can be described continuously from the shape functions $[N]$ and $[\bar{N}]$, i.e.

$$\left. \begin{aligned} \{v\} &= [N]\{v^n\}, \\ \{\bar{v}\} &= [\bar{N}]\{\bar{v}^n\}, \end{aligned} \right\} \quad (24)$$

where $\{v^n\}$ and $\{\bar{v}^n\}$ are the velocity and relative velocity vectors of the nodes, respectively. The strain rate vector $\{D\}$ can be expressed by the velocity vector $\{v^n\}$ as follows:

$$\{D\} = [B]\{v^n\}. \quad (25)$$

The strain rate-nodal velocity matrix $[B]$ is obtained by substituting the velocity fields in Eq. (24) into the strain rate-velocity relation. The variation in the quantities in Eqs. (24) and (25) are similarly given as follows:

$$\left. \begin{aligned} \{\delta v\} &= [N]\{\delta v^n\}, \\ \{\delta \bar{v}\} &= [\bar{N}]\{\delta \bar{v}^n\}, \\ \{\delta D\} &= [B]\{\delta v^n\}, \\ \text{tr}\{\delta D\} &= [B_v]\{\delta v^n\}, \end{aligned} \right\} \quad (26)$$

where the matrix $[B_v]$ denotes the relationship between the variations of the volumetric strain in element and of the nodal velocity.

The finite element discretization of Eq. (23) by

using Eqs. (24)–(26) is expressed as

$$\begin{aligned} \sum_e V_e \left\{ ([B]_e^T [C^{ep}]_e [B]_e + \rho_w [N]_e^T \{b\}_e [B_v]_e) \{du^n\}_e \right. \\ \left. - [B_v]_e^T \{dp_w\}_e \right\} \\ = \sum_e S_e^t [N]_e^T \{dt^n\}_e \\ - \sum_e S_e^c \left\{ [\bar{N}]_e^T [T]_e^T [C^f]_e [T]_e [\bar{N}]_e \{d\bar{u}^n\}_e \right. \\ \left. - dp_w [T]_e^T \{n\}_e \right\}, \quad (27) \end{aligned}$$

where $\sum_e (\)_e$ is the sum over all elements. V_e denotes the volumes of the elements. S_e^t and S_e^c are the areas of the surfaces on the traction rate boundary and the contact boundary, respectively. $[T]$ denotes the transformation matrix between the global coordinate system (x_1, x_2) and the local coordinate system (t, n) , as shown in Fig. 1. The increments of variables are given by their rates as follows:

$$\left. \begin{aligned} \{dt\} &= \{\dot{t}\} dt, \\ \{du\} &= \{v\} dt, \\ \{d\bar{u}\} &= \{\bar{v}\} dt, \\ \{dp_w\} &= \{\dot{p}_w\} dt, \\ \{dz\} &= \{\dot{z}\} dt, \end{aligned} \right\} \quad (28)$$

where dt is the time-increment.

Thus, the global stiffness equation is given from Eq. (27) as follows:

$$\begin{aligned} \left[[K] - [K^f] \right] \{du\} - \left[[L]^T - [Tn] \right] \{dp_w\} \\ = \{dF\} - [K^f] \{du^e\}, \quad (29) \end{aligned}$$

where

$$[K^f] = \sum_e S_e^c [\bar{N}]_e^T [T]_e^T [C^f]_e [T]_e [\bar{N}]_e, \quad (30)$$

$$[L] = \sum_e V_e [B_v]_e, \quad (31)$$

$$[Tn] = \sum_e S_e^c [T]_e^T \{n\}_e, \quad (32)$$

$$\{du\} = \sum_e \{du^n\}_e, \quad (33)$$

$$\{df\} = \sum_e S_e^t [N]_e^T \{dt^n\}_e, \quad (34)$$

Next, we discretize the equation of continuity for pore water (3). Here, the coupling equations (Eqs. (3) and (18)) are discretized based on the two dimensional physical model proposed by Christian and Boehmer (1970), Akai and Tamura (1978), and Asaoka et al. (1994), i.e.

$$V_e[B_v]\{du\} = \sum_{i=1}^4 q_i \{p_{wi} - p_w + \gamma_w(z_i - z)\}, \quad (35)$$

where

$$q_i = k \left(\frac{b_{x_1} l_{x_1} + b_{x_2} l_{x_2}}{(l_{x_1}^2 + l_{x_2}^2) \gamma_w} \right)_i dt, \quad (36)$$

l_{x_1} and l_{x_2} are the distance between the centers of adjacent elements along directions x_1 and x_2 , respectively. b_{x_1} and b_{x_2} are the length of the edges of the adjacent elements along directions x_1 and x_2 , respectively, as shown in Fig. 3. The four node quadrilateral isoparametric element (i.e. $i = 1 \sim 4$) is adopted in the present calculation.

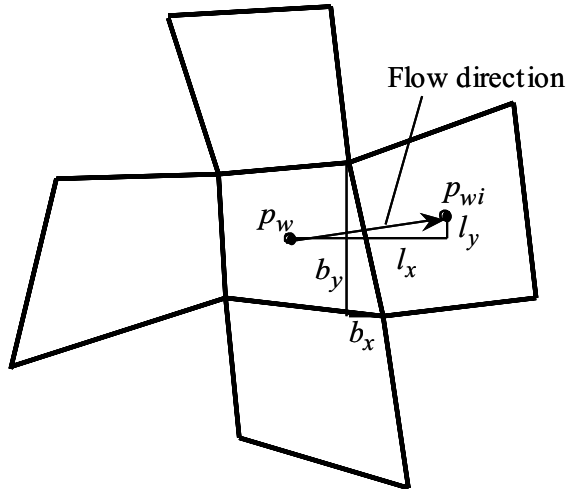


Figure 3: Physical model for pore water flow

The constraint condition with respect to the pore water flow and the deformation of skeleton of particle assembly is given from Eqs. (3), (18), (28), (31), and (35) as

$$[L]\{du\} = [q]\{dp_w\} + \{dz\}. \quad (37)$$

The incremental form of the total stiffness equation of the particle assembly-water coupled system based on the Lagrange multiplier method

with constraint conditions (29) and (37) imposed on the nodal displacements of a skeleton of particle assembly can be summarized by the following simultaneous equation:

$$\begin{bmatrix} K - K^f & -(L^T - Tn) \\ -L & q \end{bmatrix} \begin{Bmatrix} du \\ dp_w \end{Bmatrix} = \begin{Bmatrix} df \\ 0 \end{Bmatrix} - \begin{Bmatrix} 0 \\ Z \end{Bmatrix} - \begin{bmatrix} K^f & 0 \\ 0 & 0 \end{bmatrix} \begin{Bmatrix} du^e \\ 0 \end{Bmatrix}, \quad (38)$$

where the matrix $[q]$ is calculated by dividing the coefficient q_i of the term on the right-hand term in Eq. (35) by γ_w and assigning to each configurations. In this study, the differential method is adopted for the time integration of the pore water pressure and potential head, i.e.

$$\left. \begin{aligned} p_w &= \theta p_w|_{t+dt} + (1-\theta)p_w|_t, \\ z &= \theta z|_{t+dt} + (1-\theta)z|_t, \end{aligned} \right\} \quad (39)$$

where $0 \leq \theta \leq 1$.

The main objective of this study is to reveal the basic characteristics of the influence of frictional sliding on the deformation of saturated particle assembly. We adopted the traditional simple explicit finite element method, although the implicit method would be far more robust and efficient in the numerical calculation [e.g., Borja and Lee, 1990; Borja, 1991; Peric and Owen 1992; Simo and Hughes, 1997; Borja and Tamagnini, 1998; Wriggers, 2003; Larsson et al., 2004].

3 On the constitutive equations

3.1 Outline of subloading surface model

The formulation of unconventional elastoplastic constitutive equation [Drucker, 1988], which excludes the premise that the interior of a yield surface is a purely elastic domain and thus describes the plastic strain rate due to the rate of stress inside the yield surface have been attained by the subloading surface model [Hashiguchi, 1978, 1980, 1989]. This model introduces the *subloading surface*, which always passes through the current stress point and keeps the similarity to the yield surface. Then, the plastic strain rate is formulated to progress as the ratio of the size of the subloading surface to that of the yield surface increases. It fulfills the smoothness condition

[Hashiguchi, 1993a, b, 1994, 2000] and thus exhibits the *smooth elastic-plastic transition*. In this section the subloading surface model is reviewed briefly, which will be later applied to the analysis of the deformation behavior of saturated particle assembly.

3.1.1 Formulation

Let the strain rate \mathbf{D} (a symmetric part of velocity gradient \mathbf{L}) be additively decomposed into an elastic rate \mathbf{D}^e and a plastic strain rate \mathbf{D}^p , i.e.

$$\mathbf{D} = \mathbf{D}^e + \mathbf{D}^p. \quad (40)$$

The elastic strain rate \mathbf{D}^e is given by

$$\mathbf{D}^e = \mathbf{E}^{-1} \dot{\boldsymbol{\sigma}}', \quad (41)$$

where the forth-order tensor \mathbf{E} is the elastic modulus.

Let the following yield condition be assumed.

$$f(\boldsymbol{\sigma}') = F(H), \quad (42)$$

where the scalar H is the isotropic hardening/softening variable. In what follows, let it be assumed that a plastic deformation is induced by the rate of stress inside the yield surface. Then, let the yield surface described by Eq. (42) be called the *normal-yield surface*.

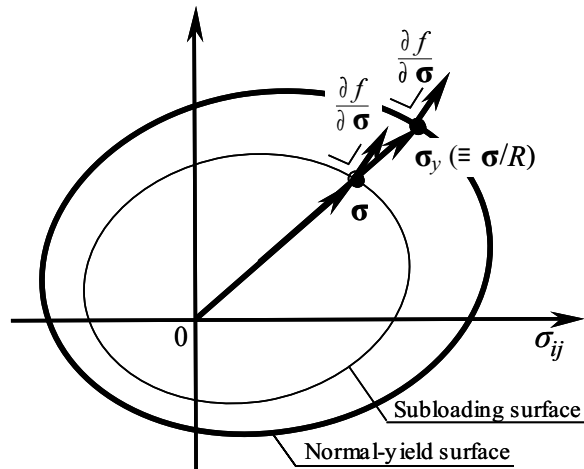


Figure 4: Normal-yield and subloading surfaces.

Now, we introduce the subloading surface, which always passes through the current stress point $\boldsymbol{\sigma}'$

and keeps a similar shape and orientation to the normal-yield surface with respect to the reference point $\mathbf{0}$ as shown in Fig. 4. The ratio of the size of subloading surface to that of normal-yield surface is called the *normal-yield ratio*, denoted by R , where $R = 0$ corresponds to the most elastic state in which the stress coincides with the similarity-center ($f = 0$), $0 < R < 1$ to the *sub-yield state* ($0 < f < F$), and $R = 1$ to the *normal-yield state* in which the stress lies on the normal-yield surface ($f = F$). Therefore, the normal-yield ratio R plays the role of three-dimensional measure of the degree of approach to the normal-yield state. Then, the subloading surface is described by

$$f(\boldsymbol{\sigma}') = RF(H). \quad (43)$$

The material-time derivative of Eq. (43) leads to

$$\text{tr}\left(\frac{\partial f(\boldsymbol{\sigma}')}{\partial \boldsymbol{\sigma}'} \dot{\boldsymbol{\sigma}}'\right) = \dot{R}F + RF' \dot{H}, \quad (44)$$

where

$$F' \equiv dF/dH. \quad (45)$$

It is assumed that the normal-yield ratio always increases with the plastic deformation, i.e.

$$\dot{R} = U(R) \|\mathbf{D}^p\| \text{ for } \mathbf{D}^p \neq \mathbf{0}, \quad (46)$$

where $\|\cdot\|$ is the magnitude, and U is a monotonically decreasing function of R fulfilling the following conditions (see Fig.5).

$$\left. \begin{array}{l} U = +\infty \quad \text{for } R = 0, \\ U = 0 \quad \text{for } R = 1, \\ (U < 0 \quad \text{for } R > 1). \end{array} \right\} \quad (47)$$

The function U fulfilling conditions (47) is simply given by

$$U = -u \ln R, \quad (48)$$

where u is a material constant.

The substitution of Eq. (46) into Eq. (44) gives rise to the *consistency condition for the subloading surface*:

$$\text{tr}\left(\frac{\partial f(\boldsymbol{\sigma}')}{\partial \boldsymbol{\sigma}'} \dot{\boldsymbol{\sigma}}'\right) = U \|\mathbf{D}^p\| F + RF' \dot{H}. \quad (49)$$

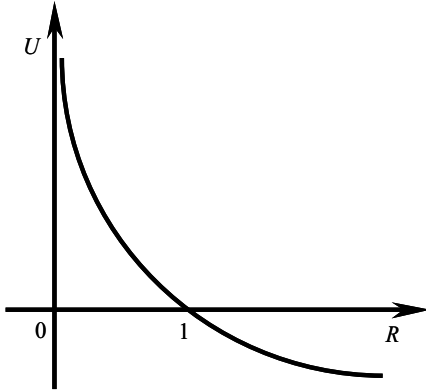


Figure 5: The function U for the evolution of normal-yield ratio R .

Assume the associated flow rule

$$\mathbf{D}^p = \lambda \mathbf{N}, \quad (50)$$

where λ is the positive proportionality factor, and the second-order tensor \mathbf{N} is the normalized outward-normal of the subloading surface, i.e.

$$\mathbf{N} \equiv \frac{\partial f(\boldsymbol{\sigma}')}{\partial \boldsymbol{\sigma}'} \Big/ \left\| \frac{\partial f(\boldsymbol{\sigma}')}{\partial \boldsymbol{\sigma}'} \right\|. \quad (51)$$

The substitution Eq. (50) into the consistency condition (49) leads to

$$\lambda = \frac{\text{tr}(\mathbf{N} \dot{\boldsymbol{\sigma}}')}{M^p}, \quad (52)$$

where the plastic modulus M^p is given by

$$M^p \equiv \left(\frac{F'}{F} h + \frac{U}{R} \right) \text{tr}(\mathbf{N} \boldsymbol{\sigma}'), \quad (53)$$

$$h \equiv \dot{H} / \lambda. \quad (54)$$

The stiffness modulus of analyzed body in Eq. (16) is given from Eqs. (40), (41), (50) and (52) as

$$\mathbf{C}^{ep} \equiv \mathbf{E} - \frac{\mathbf{E} \mathbf{N} \otimes \mathbf{N} \mathbf{E}}{M^p + \text{tr}(\mathbf{N} \mathbf{E} \mathbf{N})}, \quad (55)$$

where \otimes stands for the tensor product.

The loading criterion is given as follows:

$$\left. \begin{array}{l} \mathbf{D}^p \neq \mathbf{0} : \text{tr}(\mathbf{N} \mathbf{E} \mathbf{D}) > 0, \\ \mathbf{D}^p = \mathbf{0} : \text{tr}(\mathbf{N} \mathbf{E} \mathbf{D}) \leq 0, \end{array} \right\} \quad (56)$$

which is applicable not only to a hardening state but also to a perfectly-plastic and a softening state. The mechanical background of the loading criterion (56) has been examined in detail by Hashiguchi (1994, 2000).

3.1.2 Material functions for particle assembly

Let the stress function in the subloading surface be given as

$$f(\boldsymbol{\sigma}') = p' (1 + \chi^2), \quad (57)$$

where

$$p' \equiv -\frac{1}{3} \text{tr} \boldsymbol{\sigma}', \quad \chi \equiv \frac{\|\boldsymbol{\eta}\|}{m}, \quad \boldsymbol{\eta} \equiv \boldsymbol{\sigma}'^*, \quad (58)$$

(\cdot) * stands for the deviatoric component, m is the stress ratio $\|\boldsymbol{\eta}\|$ in the critical state, which is generally a function f_m of

$$\cos 3\theta_\eta \equiv \sqrt{6} \text{tr} \left(\frac{\boldsymbol{\eta}}{\|\boldsymbol{\eta}\|} \right)^3, \quad (59)$$

including the material constant ϕ referred to the frictional angle ϕ in the critical state for the axisymmetric compression, i.e.

$$m = f_m(\cos 3\theta_\eta; \phi). \quad (60)$$

The fulfillment of the convexity in the yield surface is desirable for the formulation of variational principles as represented by the principle of maximum plastic work [cf. e.g., Hill, 1950]. Yield surface of soils are usually formulated in the form involving an equation of the critical state surface. Therefore, the convexity of the yield surface requires that of the critical state surface, which exhibits a conical shape described approximately by the Mohr-Coulomb criterion in the principal stress space. The following equation proposed by Hashiguchi (2002) is adopted as the function m fulfilling the aforementioned requirements.

$$m \equiv \frac{14 \sqrt{6} \sin \phi}{(3 - \sin \phi)(8 + \cos 3\theta_\eta)}. \quad (61)$$

The normal-yield surface for Eq. (57) is exhibited by the ellipsoid in the $(p', \|\boldsymbol{\sigma}'^*\|)$ plane (Fig. 6), i.e.

$$\left(\frac{p' - F/2}{F/2} \right)^2 + \left(\frac{\|\boldsymbol{\sigma}'^*\|}{mF/2} \right)^2 = 1. \quad (62)$$

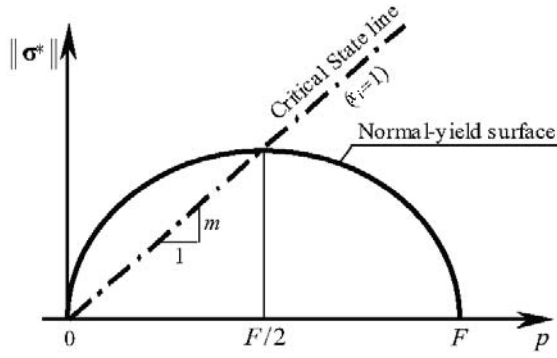


Figure 6: Normal-yield surface for the isotropic particle assembly.

The isotropic hardening/softening of soils is substantially induced by the decrease/increase of plastic volumetric strain ε_v^p . The isotropic hardening/softening function F is given from the $\ln v - \ln p'$ linear relation (v : volume) for the isotropic consolidation [Hashiguchi, 1995] as follows:

$$F = (F_0 + p_e) \exp\left(\frac{H}{\rho - \gamma}\right) - p_e, \quad H = -\varepsilon_v^p, \quad (63)$$

where F_0 is the initial value of F . ρ and γ are the material constants describing the slopes of the normal-consolidation and swelling lines, respectively, in the $(\ln v, \ln p')$ plane. p_e is the material constant leading to $v \rightarrow \infty$ for $p' \rightarrow -p_e$.

The elastic modulus \mathbf{E} in Eq. (41) is given in the Hook's type as follows:

$$E_{ijkl} = \left(K - \frac{2}{3}G\right) \delta_{ij} \delta_{kl} + G(\delta_{ik} \delta_{jl} + \delta_{il} \delta_{jk}), \quad (64)$$

where δ_{ij} is Kronecker's delta with $\delta_{ij} = 1$ ($i = j$) and $\delta_{ij} = 0$ ($i \neq j$). The elastic bulk modulus K and the elastic shear modulus G are given as

$$K = \frac{p' + p_e}{\gamma}, \quad (65)$$

$$G = \frac{3(1-2\nu)}{2(1+\nu)} K, \quad (66)$$

where ν is Poisson's ratio.

3.2 Outline of the subloading-friction model

The subloading-friction model [Hashiguchi et al., 2005] is formulated by incorporating the concept of the subloading surface to the conventional friction model, while the friction phenomenon is similar to the deformation behavior of frictional material described in 3.1. In this section the subloading-friction model is reviewed briefly, which will be later applied to the analysis of the frictional contact phenomenon.

3.2.1 Formulation

The relative velocity $\bar{\mathbf{v}}$ between contact surfaces is additively decomposed into the normal component $\bar{\mathbf{v}}_n$ and the tangential component $\bar{\mathbf{v}}_t$ as follows:

$$\bar{\mathbf{v}} = \bar{\mathbf{v}}_n + \bar{\mathbf{v}}_t \quad (67)$$

with

$$\left. \begin{aligned} \bar{\mathbf{v}}_n &= (\bar{\mathbf{v}} \cdot \mathbf{n}) \mathbf{n} = (\mathbf{n} \otimes \mathbf{n}) \bar{\mathbf{v}}, \\ \bar{\mathbf{v}}_t &= \bar{\mathbf{v}} - \bar{\mathbf{v}}_n = (\mathbf{I} - \mathbf{n} \otimes \mathbf{n}) \bar{\mathbf{v}}. \end{aligned} \right\} \quad (68)$$

Furthermore, it is assumed that $\bar{\mathbf{v}}$ is additively decomposed into the elastic part $\bar{\mathbf{v}}^e$ and the plastic part, i.e. *sliding velocity* $\bar{\mathbf{v}}^p$:

$$\bar{\mathbf{v}} = \bar{\mathbf{v}}^e + \bar{\mathbf{v}}^p. \quad (69)$$

First, let the elastic part be given by

$$\dot{\mathbf{f}}' = \dot{\mathbf{f}}'_n + \dot{\mathbf{f}}'_t = -\mathbf{C}^e \bar{\mathbf{v}}^e, \quad (70)$$

where

$$\mathbf{C}^e = \mathbf{C}_n^e + \mathbf{C}_t^e, \quad (71)$$

\mathbf{f}'_n and \mathbf{f}'_t are the normal and the tangential components of the effective traction vector \mathbf{f}' . The second-order tensor \mathbf{C}^e is the elastic modulus between contact surfaces, i.e.

$$\left. \begin{aligned} \mathbf{C}_n^e &= \alpha_n \mathbf{n} \otimes \mathbf{n}, \\ \mathbf{C}_t^e &= \alpha_t (\mathbf{I} - \mathbf{n} \otimes \mathbf{n}), \end{aligned} \right\} \quad (72)$$

where α_n and α_t are penalty parameters representing elastic fictitious moduli in the normal and the tangential directions to the contact surface.

Let the following sliding-yield surface with isotropic hardening/softening, which describes the sliding condition be assumed.

$$\bar{f}(\|\mathbf{f}'_n\|, \|\mathbf{f}'_t\|) = \bar{F}(\bar{H}), \quad (73)$$

where the \bar{H} is the isotropic hardening/softening variable, which prescribes the expansion/contraction of the sliding surface.

In what follows, we assume that the interior of the sliding-yield surface is not a purely elastic domain but the sliding velocity is induced by the rate of traction inside that surface. Therefore, let the surface described by Eq. (73) be renamed as the *normal-sliding surface*. Then, we introduce the *sliding-subloading surface*, which always passes through the current traction point \mathbf{f}' and keeps a similar shape and orientation to the normal-sliding surface with respect to the null traction point $\mathbf{f}' = \mathbf{0}$. Let the ratio of the size of sliding-subloading surface to that of the normal-sliding surface be called the *normal-sliding ratio*, and let it be denoted by \bar{R} . Thus, the sliding-subloading surface is described by

$$\bar{f}(\|\mathbf{f}'_n\|, \|\mathbf{f}'_t\|) = \bar{R}\bar{F}(\bar{H}), \quad (74)$$

where $\bar{R} = 0$ corresponds to the null traction state ($\bar{f} = 0$) as the most elastic state, $0 < \bar{R} < 1$ to the *sub-sliding state* ($0 < \bar{f} < \bar{F}$), and $\bar{R} = 1$ to the *normal-sliding state* in which the traction lies on the normal-sliding surface ($\bar{f} = \bar{F}$). Therefore, the normal-sliding ratio \bar{R} plays the role of a three-dimensional measure of the degree of approach to the normal-sliding state.

It can be assumed that \bar{R} increases with the sliding velocity, i.e.

$$\dot{\bar{R}} = \bar{U}(\bar{R})\|\bar{\mathbf{v}}^p\| \text{ for } \bar{\mathbf{v}}^p \neq \mathbf{0}, \quad (75)$$

where \bar{U} is the monotonically decreasing function of \bar{R} fulfilling the following conditions.

$$\left. \begin{array}{l} \bar{U} = +\infty \quad \text{for } \bar{R} = 0, \\ \bar{U} = 0 \quad \text{for } \bar{R} = 1, \\ (\bar{U} < 0 \quad \text{for } \bar{R} > 1). \end{array} \right\} \quad (76)$$

The function \bar{U} fulfilling conditions (76) is simply given by

$$\bar{U} = -\bar{u} \ln \bar{R}, \quad (77)$$

where \bar{u} is a material constant.

The substitution of Eq. (75) into the material-time derivative of Eq. (74) gives rise to the *consistency condition for the sliding-subloading surface*:

$$\frac{\partial \bar{f}}{\partial \|\mathbf{f}'_n\|} \mathbf{n} \cdot \dot{\mathbf{f}}'_n + \frac{\partial \bar{f}}{\partial \|\mathbf{f}'_t\|} \mathbf{t} \cdot \dot{\mathbf{f}}'_t = \bar{U} \|\bar{\mathbf{v}}^p\| \bar{F} + \bar{R} \dot{\bar{F}}, \quad (78)$$

where

$$\mathbf{n} = \frac{\mathbf{f}'_n}{\|\mathbf{f}'_n\|}, \quad \mathbf{t} = \frac{\mathbf{f}'_t}{\|\mathbf{f}'_t\|}. \quad (79)$$

Assume the following *sliding flow rule*.

$$\bar{\mathbf{v}}^p = -\bar{\lambda} \mathbf{t} \quad (\bar{\lambda} > 0), \quad (80)$$

where $\bar{\lambda}$ is the positive proportionality factor. In this study, we assumed no dilatancy with respect to plastic sliding, although the generalized sliding flow rule was discussed by several researchers [e.g., Michalowski and Mroz, 1978; Curnier, 1984; Hashiguchi et al., 2005].

By substituting of Eqs. (67), (69), (72) and (80) into Eq. (78), the proportionality factor $\bar{\lambda}$ expressed in terms of the relative velocity, rewriting it as $\bar{\Lambda}$, is given by

$$\bar{\Lambda} = \frac{-\left(\alpha_n \frac{\partial \bar{f}}{\partial \|\mathbf{f}'_n\|} \mathbf{n} + \alpha_t \frac{\partial \bar{f}}{\partial \|\mathbf{f}'_t\|} \mathbf{t}\right) \cdot \bar{\mathbf{v}}}{\bar{R}\bar{F}'\bar{h} + \bar{U}\bar{F} + \alpha_t \frac{\partial \bar{f}}{\partial \|\mathbf{f}'_t\|}}, \quad (81)$$

where \bar{h} is the homogeneous degree-one function of \bar{H} and \mathbf{t} , which is related to $\dot{\bar{H}}$ as

$$\bar{F}' = \frac{d\bar{F}}{d\bar{H}}, \quad \bar{h} = \frac{\dot{\bar{H}}}{\bar{\lambda}}. \quad (82)$$

The frictional stiffness modulus in Eq. (17) is given from Eqs. (67)-(72), (80) and (81) as

$$\mathbf{C}^f \equiv \mathbf{C}^e + \frac{\alpha_t \mathbf{t} \otimes \left(\alpha_n \frac{\partial \bar{f}}{\partial \|\mathbf{f}'_n\|} \mathbf{n} + \alpha_t \frac{\partial \bar{f}}{\partial \|\mathbf{f}'_t\|} \mathbf{t}\right)}{\bar{R}\bar{F}'\bar{h} + \bar{U}\bar{F} + \alpha_t \frac{\partial \bar{f}}{\partial \|\mathbf{f}'_t\|}}. \quad (83)$$

For the case of $\bar{F} = \text{const.}$, Eq. (83) becomes

$$\mathbf{C}^f \equiv \mathbf{C}^e + \frac{\alpha_t \mathbf{t} \otimes \left(\alpha_n \frac{\partial \bar{f}}{\partial \|\mathbf{f}'_n\|} \mathbf{n} + \alpha_t \frac{\partial \bar{f}}{\partial \|\mathbf{f}'_t\|} \mathbf{t}\right)}{\bar{U}\bar{F} + \alpha_t \frac{\partial \bar{f}}{\partial \|\mathbf{f}'_t\|}}. \quad (84)$$

The loading criterion for the sliding velocity is given as follows:

$$\left. \begin{array}{l} \bar{\mathbf{v}}^p \neq \mathbf{0} : \bar{\Lambda} > 0, \\ \bar{\mathbf{v}}^p = \mathbf{0} : \bar{\Lambda} \leq 0 \end{array} \right\} \quad (85)$$

due to the requirement of positiveness for the proportionality factor $\bar{\Lambda}$ [Hashiguchi et al., 2005].

The sliding velocity is obtained by substituting the sliding flow rule (80) into the consistency condition (78), which is obtained by incorporating the evolution rule (75) of the normal-sliding ratio \bar{R} into the material-time derivative of Eq. (74) for the sliding-subloading surface. Then, the sliding velocity progresses gradually as the traction approaches the normal-sliding surface, exhibiting a smooth elastic-plastic transition. Thus, it fulfills the smoothness condition. Therefore, the subloading-friction model has the following notable advantages: In the numerical calculation, the traction is automatically drawn back to the normal-sliding surface even if it goes out from that surface since it is formulated such that $\dot{\bar{R}} > 0$ for $\bar{R} < 1$ and $\dot{\bar{R}} < 0$ for $\bar{R} > 1$ in Eq. (75) with condition (76) as illustrated in Fig. 7. Thus, the subloading-friction model allows a rough numerical calculation with large loading steps even in numerical calculation.

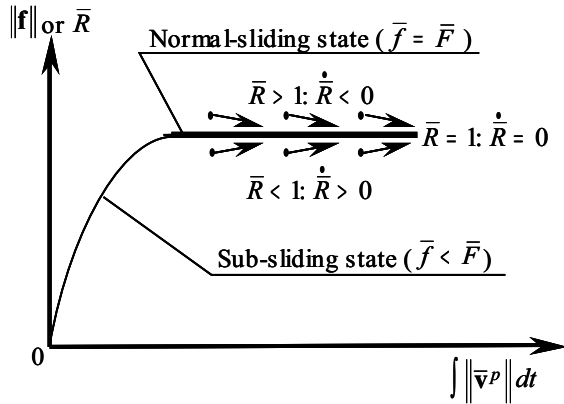


Figure 7: Automatic controlling function causes the traction to approach the normal-sliding surface in the plastic frictional loading process.

In conventional models, on the other hand, a special algorithm has to be incorporated for pulling

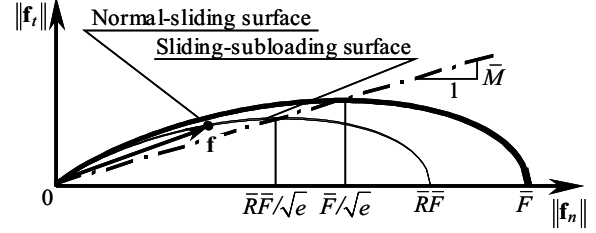


Figure 8: Tear-shaped normal-sliding and sliding-subloading surfaces of Eq. (86).

the traction back to the sliding-yield surface so as not to go out from the surface in numerical calculation.

3.2.2 Material function for sliding-yield surface

Let the following tear-shaped surface be assumed to the normal-sliding and sliding-subloading surfaces (Fig. 8), which was proposed by Hashiguchi et al. (2005):

$$\bar{f}(\|\mathbf{f}'_n\|, \|\mathbf{f}'_t\|) = \|\mathbf{f}'_n\| \exp\left(\frac{\bar{\chi}^2}{2}\right), \quad (86)$$

where

$$\bar{\eta} \equiv \frac{\|\mathbf{f}'_t\|}{\|\mathbf{f}'_n\|}, \quad \bar{\chi} \equiv \frac{\bar{\eta}}{\bar{M}}. \quad (87)$$

\bar{M} is a material constant depending on the frictional property.

4 Conditions of numerical experiments

The one-dimensional consolidation test referred to as *oedometer* at a constant strain rate is one of the popular laboratory tests for measurement of properties of saturated particle assembly. The results of the consolidation tests, however, are affected by the frictional sliding characteristics between soil specimen and steel ring through the skin packing the soil specimen even if friction reduction treatments are performed. The influence of the friction will be examined below by numerical experiments.

The finite element mesh and boundary conditions for the compaction test at a constant strain rate of soil specimen are shown in Fig. 9. Here, the analysis is performed on an axisymmetric condition

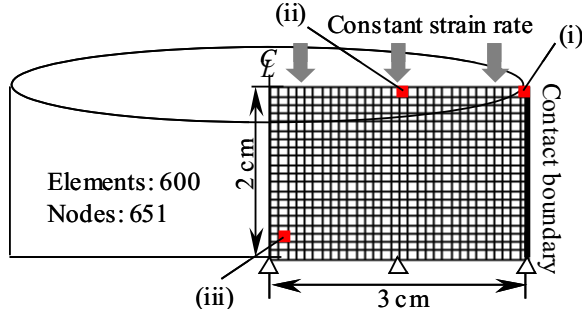


Figure 9: FE mesh and boundary condition.

since the test specimen is of the circular shape. The analytical specimen has 3 cm in radius and of 2 cm in height. The bottom and top of the specimen are set under undrained and drained boundary conditions, respectively, and set under non-friction condition. In addition, the periphery of the specimen is under a contact boundary condition with the steel ring (Here, we neglect the skin packing). The constant strain rate (0.03%/min) is applied to the over-consolidated clay (OCR = 10; i.e. initial $R = 0.1$) until the pressure on the upper surface reaches 640 kPa. In order to examine the influence on the interaction behavior due to the frictional sliding, we assume the following conditions.

1. The specimen is initially assumed to uniform over the whole body under the isotropic state of stress.
2. The initial tangential traction is neglected and the initial normal traction between the clay and the steel ring is uniformly distributed over the boundary, which is equal to the horizontal normal stress of the clay, and thus the initial normal-sliding ratio \bar{R} is uniform over the specimen.

On the other hand, the skin covering the clay specimen contributes the reduction of friction between the clay specimen and the steel ring. Then, we adopt the following conditions for friction in order to examine the influence of friction reduction by the lubricated skin.

1. The frictional property is described originally by the material constant \bar{M} . We then

set the following three values: (a) $\bar{M} = 0.0$ without friction (idealized nonfrictional condition), (b) $\bar{M} = 0.01$ with reduction treatment of friction and (c) $\bar{M} = 0.1$ without reduction treatment of friction.

2. To examine the influence of the frictional sliding behavior induced by the rate of traction inside the normal-sliding surface, we adopt the frictional conditions of two patterns: (a) the subloading-friction model ($\bar{u} = 10$) and (b) the conventional friction model ($\bar{u} \rightarrow \infty$), fixing the frictional property as $\bar{M} = 0.1$ in order to clarify the influence.

Table 1: Material parameters.

(a) Subloading surface model

F_0 (kPa)	1	u	10
ν	0.33	ϕ (deg.)	36.4
ρ	0.08	k (m/s)	1.0×10^{-8}
γ	0.008	γ_g (kN/m ²)	16

(b) Subloading-friction model

\bar{F} (kPa)	265	\bar{M}	0.01, 0.1
α_t, α_n (MPa)	1000	\bar{u}	10, 1000 ($\approx \infty$)

The material parameters for the elastoplastic deformation behavior of clay and the friction on the boundary surface are shown in Tab. 1, while we assume that the body force \mathbf{b} can be neglected in the consolidation test.

The five material constants of \bar{F} , \bar{M} , \bar{u} , α_n and α_t are included in the present friction model. The mechanical meanings and/or determination of material parameters is first described briefly as follows:

- 1) \bar{F} is the size of sliding-yield surface and is realized in the state that the peak traction is saturated by the conventional friction model ($\bar{u} \rightarrow \infty$).
- 2) \bar{M} is the traction ratio $\|\mathbf{f}'_t\|/\|\mathbf{f}'_n\|$ at the highest point of tangential traction on the normal-sliding surface.
- 3) \bar{u} characterizes the gentleness of the traction vs. sliding displacement curve. The curve

sharply-bent at the sliding-yield point is described for an infinite value of \bar{u} for which the behavior of the present model reduces to the conventional friction model. On the other hand, a more gentle curve is described by a smaller value of \bar{u} .

- 4) α_n and α_t characterize the elastic property in contact surface in the normal and tangential direction, respectively, which are determined by the initial part of the traction vs. sliding displacement curve before a plastic-sliding is induced.

5 Results and discussion

5.1 Effects on the reduction treatment of friction

The contours of the pore water pressure p_w and volumetric strain ϵ_v in the final stage of loading are shown in Figs. 10 and 11, respectively for three cases of friction, i.e. (a) nonfriction; (b) $\bar{M} = 0.01$, $\bar{u} = 10$; and (c) $\bar{M} = 0.1$, $\bar{u} = 10$. The pore water pressure is distributed uniformly along the horizontal direction for (a) with nonfriction. On the other hand, it becomes to distribute nonuniformly as it rapidly increase in the part nearer the contact boundary and the drained boundary for (b) and (c) with friction. Especially, these behaviors are more remarkable for the higher value of \bar{M} .

The distribution of volumetric strain is similar to that of the pore pressure described above.

The contours of the magnitude of the deviatoric strain $\|\epsilon^*\|$ in the final stage of loading are shown in Fig. 12 for three cases of friction. Although the deviatoric strain is distributed uniformly under frictional conditions (a) and (b), as it increases more quickly in the part nearer side-edge at the drained boundary.

It is understood that the element behavior of the specimen is drastically improved by the friction reduction treatments such as greases and lubricants. Moreover, from this analysis, it is expected that a prediction of the region that satisfies the element behavior in the consolidation test is possible.

The distributions of tangential tractions and rela-

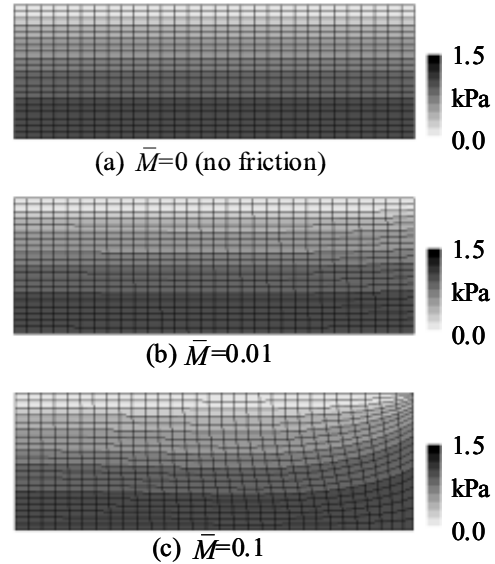


Figure 10: Contours of pore water pressure when the loading is completed ($\bar{u} = 10$).

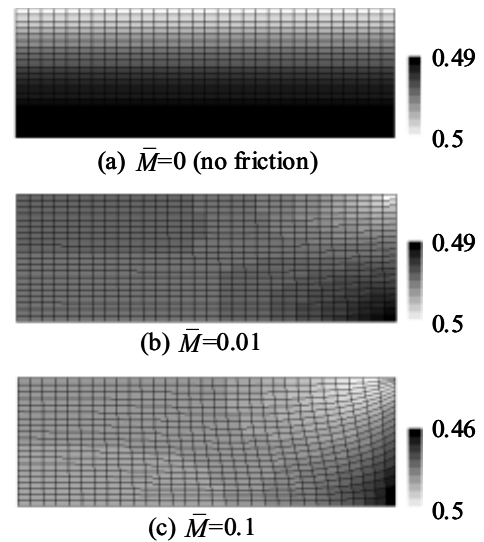


Figure 11: Contours of volumetric strain when the loading is completed ($\bar{u} = 10$).

tive displacements on the contact boundary in the final stage of loading are shown in Fig. 13. The tangential traction increases as \bar{M} does, and it is larger in the part nearer the top of the ring.

The relative displacement increases of course linearly along the vertical wall of the ring with a low friction. On the other hand, it is suppressed in the middle part and thus it is distributed nonlinearly

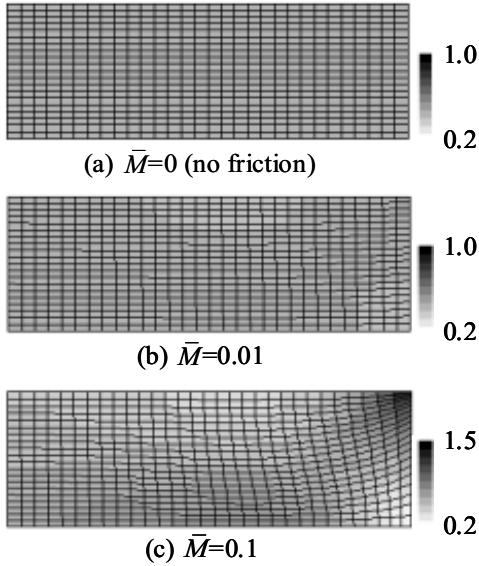


Figure 12: Contours of the magnitude of deviatoric strain when the loading is completed ($\bar{u} = 10$).

for a high friction. Thus, it is confirmed that the frictional sliding phenomenon induces the non-uniform pore water pressure and the deformation of specimen.

In order to examine the abovementioned facts in a more detail, the variations of pore water pressure p_w with an elapsed time in typical reference elements (i)–(iii) in Fig. 9 are shown in Fig. 14. For the case (c) of high friction the dissipation of the pore water pressure is slow in the elements (ii) and (iii) as compared to that in the element (i) at the contact boundary. The reason for this behavior is considered as follows: the element (i), as compared to the internal element (ii), is compacted by the frictional resistance on the contact boundary and the pore water flow horizontally toward the center of the specimen. The variations of the magnitude of deviatoric strain $\|\epsilon^*\|$ with an elapsed time in the three reference elements (i)–(iii) in Fig. 9 are shown in Fig. 15. The larger deviatoric strain is induced in the element (i) by the frictional resistance at the contact boundary. Thus, the oedometer test cannot be regarded as an element test but should be regarded a boundary value problem as seen in the result for condition (c) of high friction. On the other hand, when \bar{M} is

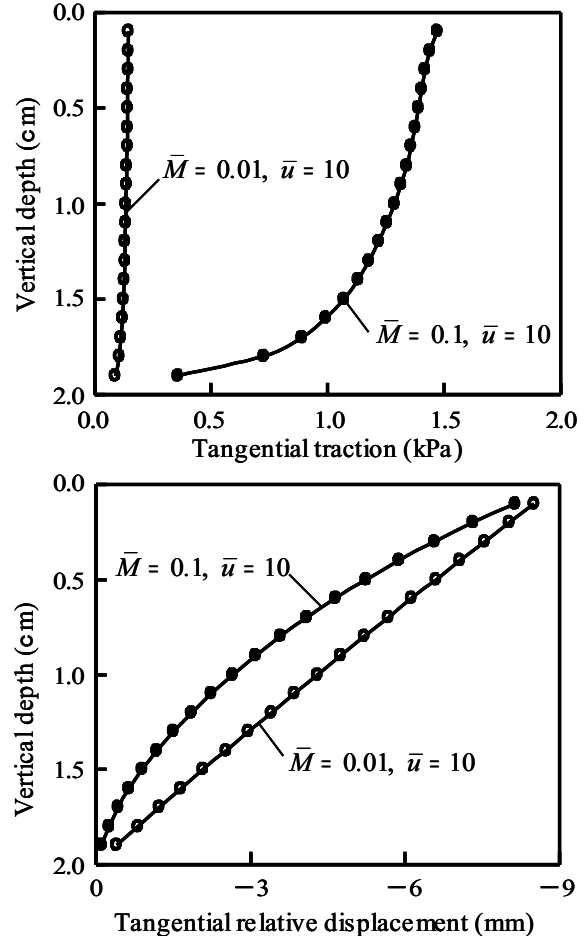


Figure 13: Distributions of tangential tractions and relative displacements on the contact boundary.

small, the variation in the strain reveals an almost similar path with the elapsed time. The friction reduction treatment would be important for the improvement in the accuracy of oedometer test.

5.2 Comparison of the subloading-friction model with the conventional model

The distributions of tangential tractions and relative displacements on the contact boundary at the end of loading process are shown in Fig. 16, where the calculated results for the subloading-friction model ($\bar{u} = 10$), and the conventional friction model ($\bar{u} \rightarrow \infty$) are shown. The high tangential traction is predicted by the conventional friction model since the tangential traction for the sliding-yield condition is predicted even for a null

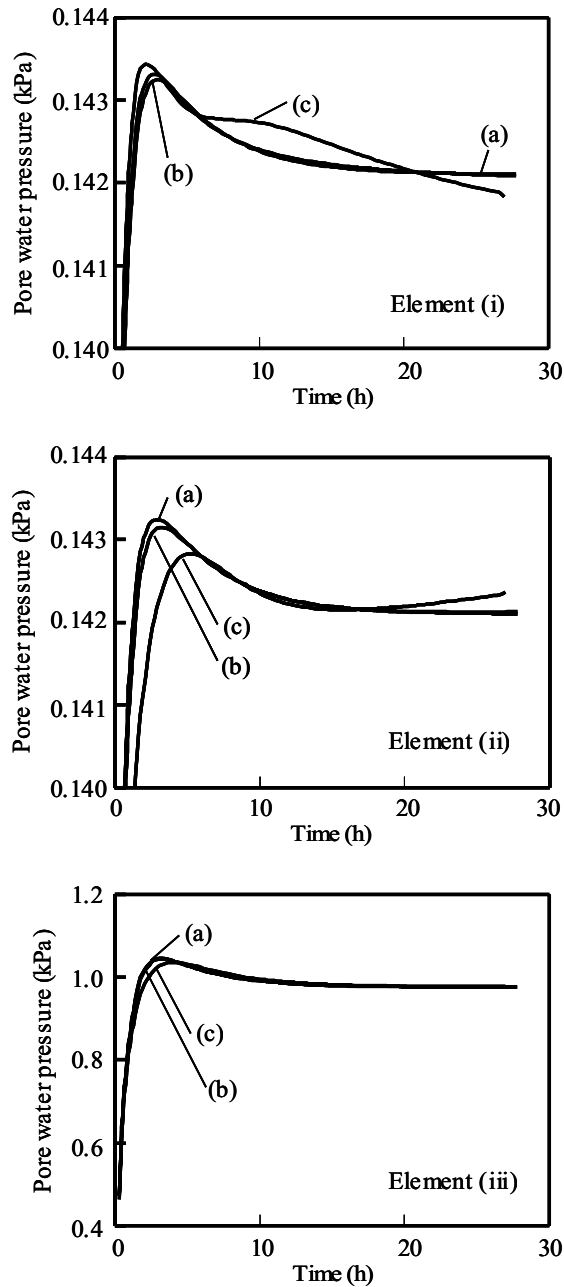


Figure 14: Variations of pore water pressure in the reference elements with an elapsed time during loading.

or infinitesimal tangential relative displacement. On the other hand, a smooth tangential traction is predicted by the subloading-friction model. Furthermore, the distribution of tangential displacement is larger for smaller values of \bar{u} in the evolution rule of the normal-sliding ratio.

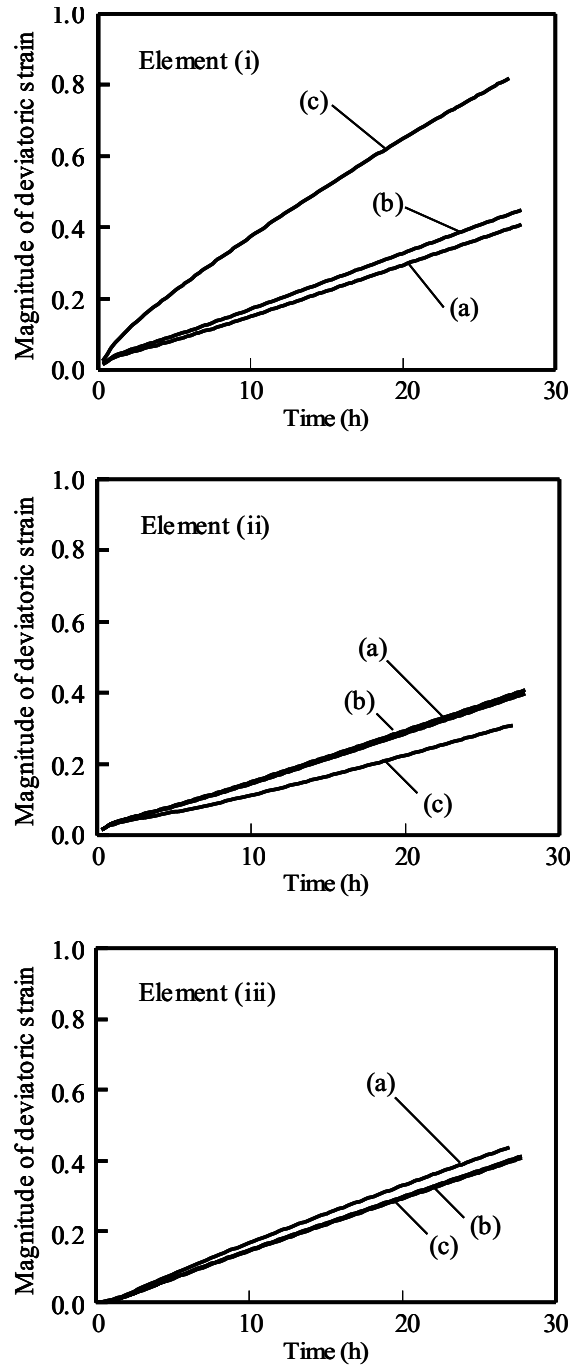


Figure 15: Variations of magnitude of deviatoric strain in the reference elements with an elapsed time during loading.

The relationships between the total normal and the total tangential forces on the entire contact boundary vs. the compression of the specimen are shown in Fig. 17 for the subloading-friction

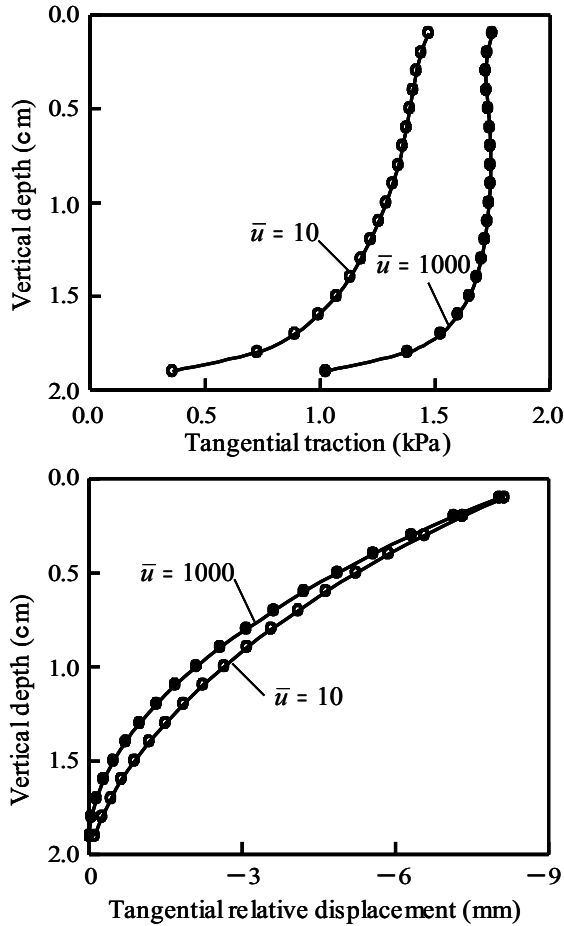


Figure 16: Distributions of tangential tractions and relative displacements on the contact boundary.

model ($\bar{u} = 10$) and for the conventional friction model ($\bar{u} \rightarrow \infty$). It is observed that the smaller total tangential force is predicted for the smaller value of the material constant \bar{u} . On the other hand, the total normal force is predicted to be almost identical independent of the value of \bar{u} .

The variations of the magnitude of the deviatoric strain $\|\mathbf{e}^*\|$ in the reference elements (i)–(iii) in Fig. 9 with an elapsed loading time for two levels of the material constant \bar{u} are shown in Fig. 18. The variation of the deviatoric strain is influenced by the value of \bar{u} such that larger value is predicted by the conventional friction model than by the subloading-friction model. It is caused by the fact that the tangential displacement is not allowed by the conventional friction model until the

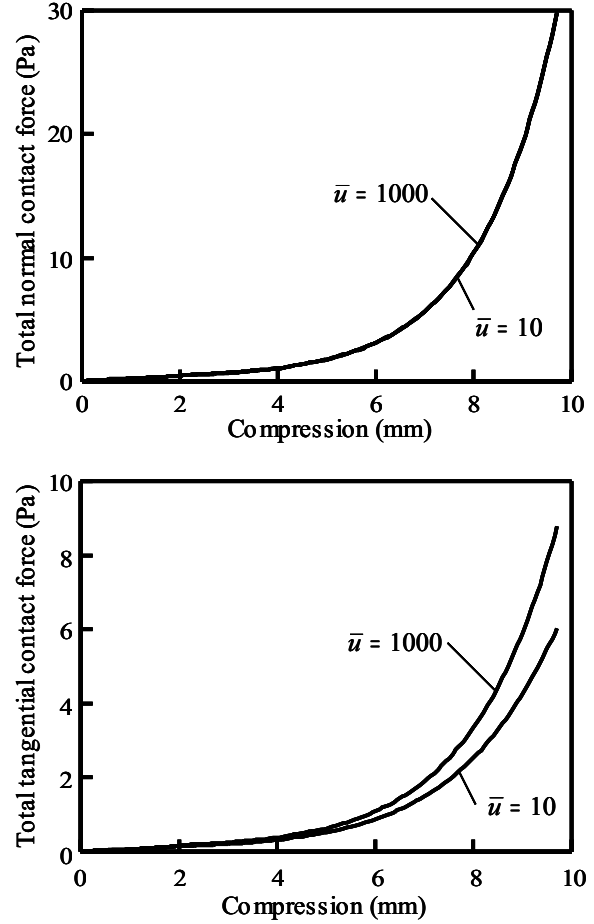


Figure 17: Relationships between the total normal, the total tangential contract forces and the compression of the specimen.

tangential traction reaches the sliding-yield surface. Thus, the prediction of sliding displacement below the normal-sliding surface would be of importance for the accurate analysis of particle assembly-coupled contact problems.

6 Concluding remarks

In order to analyze accurately the elastoplastic deformation phenomenon of saturated particle assembly considering the friction phenomenon at the contact boundary, the particle assembly-water coupled finite element program is developed by incorporating both the subloading surface and subloading-friction models in this article. It is then applied to the analysis of the compaction phenomena of saturated clay at a constant

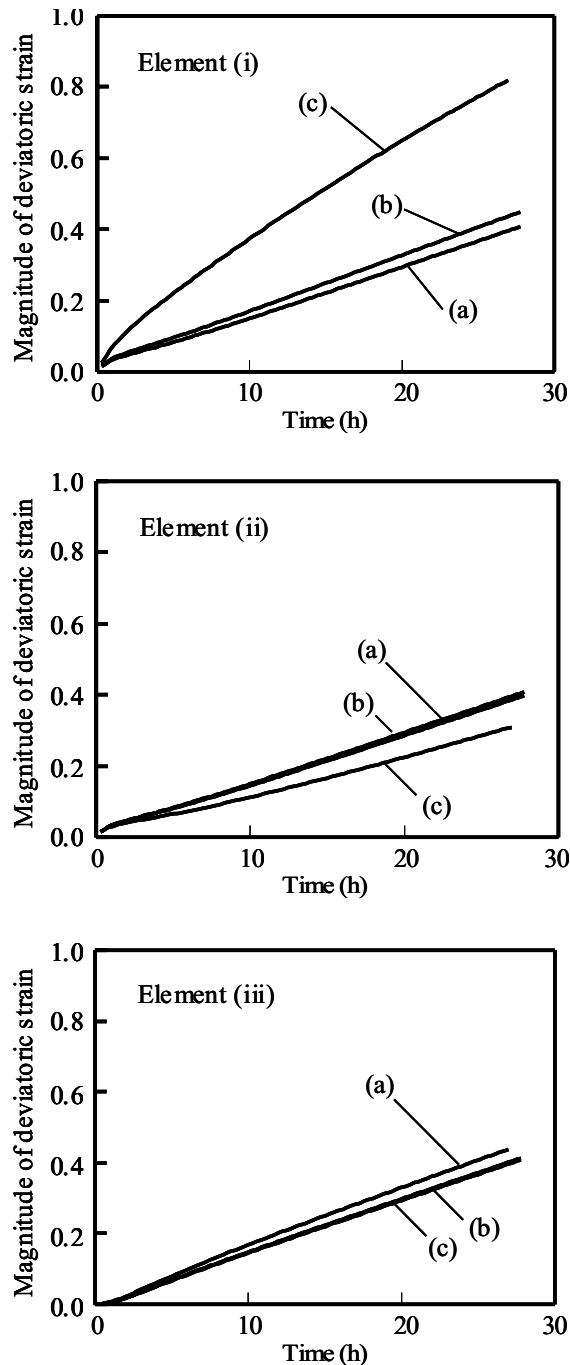


Figure 18: Variations of magnitude of deviatoric strain in the reference elements with an elapsed time during loading.

strain rate as an example of the typical particle assembly-water coupled contact problem. The following facts are revealed from the analysis.

- i) The frictional sliding phenomenon at the contact boundary as well as pore water flow in the particle assembly influences significantly the deformation behavior.
- ii) Further the occurrence of sliding displacement below the normal-sliding surface affects the deformation of particle assembly.
- iii) Then, strictly speaking, the oedometer test which is one of the most standard tests for soil behavior cannot be regarded as the element test revealing merely constitutive behavior but has to be improved to reduce the friction at the wall of specimen container.

The proposed method and finite element program could be applied widely to the analyses of general particle assembly-water coupled contact problem in the fields of geotechnical and chemical engineering.

References

- Akai, K.; Tamura, T.** (1978): Numerical analysis of multidimensional consolidation accompanied with elasto-plastic constitutive equation. *Proc. of JSCE*, No.269, pp.95-104 (in Japanese).
- Asaoka, A.; Nakano, M.; Noda, T.** (1994): Soil-water coupled behavior of saturated clay near/at critical state. *Soils and Foundations*, Vol.34, No.1, pp.91-105.
- Asaoka, A.; Nakano, M.; Noda, T.** (1995): Imperfection sensitive bifurcation of Cam-Clay under plane strain compression with undrained boundaries. *Soils and Foundations*, Vol.35, No.1, pp.83-100.
- Asaoka, A.; Nakano, M.; Noda, T.** (1997): Soil-water coupled behavior of heavily overconsolidated clay near/at critical state. *Soils and Foundations*, Vol. 37, pp. 13-39.
- Asaoka, A.; Noda, T.; Kaneda, K.** (1998): Displacement/Traction boundary conditions represented by constraint condition on velocity field of soil. *Soil and foundations*, Vol.38, No.4, pp.173-181.
- Asaoka, A.; Nakano, M.; Noda, T.; Kaneda, K.** (2000): Delayed compression/consolidation of

natural clay due to degradation of soil structure. *Soils and Foundations*, Vol.40, No.3, pp.75-85.

Borja, R.I.; Lee, S.R. (1990): Cam-Clay plasticity, Part I: Implicit integration of elasto-plastic constitutive relations. *Comput. Methods Appl. Mech. Engrg.* Vol.78, pp. 49–72.

Borja, R.I. (1991): Cam-Clay plasticity, Part II: Implicit integration of constitutive equation based on a nonlinear elastic stress predictor. *Comput. Methods Appl. Mech. Engrg.* Vol. 88, pp. 225–240.

Borja, R.I.; Tamagnini, C. (1998): Cam-Clay plasticity, Part III: Extension of the infinitesimal model to include finite strains. *Comput. Methods Appl. Mech. Engrg.* Vol.155, pp.73–95.

Cheng, J-H.; Kikuchi, N. (1985): An incremental constitutive relation of uniaxial contact friction for large deformation analysis. *J. Applied Mechanics (ASME)*, Vol. 52, pp.639-648.

Cristian, J. T. (1968): Undrained stress distribution by numerical methods. *Proc. ASCE, SM6*, pp.1333-1345.

Cristian, J. T.; Boehrer, J. W. (1970): Plane strain consolidation by finite elements. *Proc. ASCE, SM6*, pp.1435-1457.

Courtney-Pratt, J.S.; Eisner, E. (1957): The effect of a tangential force on the contact metallic bodies. *Proc. Royal Soci. London, Ser. A*, Vol.238, pp.529-550, 1957

Curnier, A. (1984): A theory of friction. *Int. J. Solids and Structures*, Vol.20, pp.637-647.

Desai, C.S.; Zaman, M.M.; Drumm, E.C. (1985): Cyclic testing and modeling of interfaces. *J. Geotech. Eng.*, Vol.111, pp.793-815.

Drucker, D.C. (1988): Conventional and unconventional plastic response and representation. *J. Applied Mechanics Reviews (ASME)*, Vol.41, pp.151-167.

Ferguson, W.J.; Palanathakumar, B. (2005): A fully coupled finite element model of landfill gas migration in a partially saturated soil. *CMES: Computer Modeling in Engineering & Sciences*, Vol.8, pp201-215.

Hagman, L.; Olofsson, U. (1998): A model for micro-slip between flat surfaces based on defor-

mation of ellipsoidal elastic asperities-parametric study and experimental investigation. *Tribology International*, Vol.31, pp.209-217.

Hashiguchi, K. (1978): Plastic constitutive equations of granular materials. *Proc. US-Japan Seminar Continuum Mech. Stast. Appr. Mech. Granular Materials*, Sendai, pp. 321-329.

Hashiguchi, K. (1980): Constitutive equations of elastoplastic materials with elastic-plastic transition. *J. Applied Mechanics (ASME)*, Vol.47, pp.266-272.

Hashiguchi, K. (1989): Subloading surface model in unconventional plasticity. *Int. J. Solids and Structures*, Vol.25, pp.917-945.

Hashiguchi, K. (1993a): Fundamental requirements and formulation of elastoplastic constitutive equations with tangential plasticity. *Int. J. Plasticity*, Vol. 9, pp. 525-549.

Hashiguchi, K. (1993b): Mechanical requirements and structures of cyclic plasticity models. *Int. J. Plasticity*, Vol. 9, pp. 721-748.

Hashiguchi, K. (1994): On the loading criterion, *Int. J. Plasticity*, Vol.10, pp.871-878.

Hashiguchi, K. (1995): On the linear relations of $V\text{-ln}p$ and $\ln v\text{-ln}p$ for isotropic consolidation of soils. *Int. J. Numer. Anal. Method. Geomech.*, Vol.19, pp.367-376.

Hashiguchi, K. (2000): Fundamentals in constitutive equation -Continuity and smoothness conditions and loading criterion. *Soils and Foundations*, Vol.40, pp.155-161.

Hashiguchi, K. (2002): A Proposal of the simplest convex-conical surface for soils. *Soils and Foundations*, Vol.42, pp.107-113.

Hashiguchi, K.; Ozaki, S.; Okayasu, T. (2005): Unconventional friction theory based on the subloading surface concept. *Int. J. Solids and Structures*, Vol.42, pp.1705-1727.

Hill, R. (1950): *The mathematical theory of plasticity*, Clarendon Press.

Kikuchi, N.; Oden, J. T. (1988): *Contact problem in elasticity*, A study of variational inequalities and finite element methods. SIAM, Philadelphia.

Liu, X.; Scarpas, A. (2005): Numerical model-

ing of the influence of water suction on the formation of strain localization in saturated sand. *CMES: Computer Modeling in Engineering & Sciences*, Vol.9, pp.57-74.

Larsson, J.; Faleskog, J.; Massih, A.R. (2004): Analysis of densification and swelling of solids using pressure dependent, plasticity criteria, *CMES: Computer Modeling in Engineering & Sciences*, vol.5, pp.73-80.

Michalowski, R; Mroz, Z. (1978): Associated and non-associated sliding rules in contact friction problems. *Arch. Mech.*, Vol.30, pp.259-276.

Olofsson, U. (1995): Cyclic micro-slip under unlubricated conditions. *Tribology International*, Vol.28, pp.207-217.

Olofsson, U.; Hagman, L. (1997): A model for micro-slip between flat surfaces based on deformation of ellipsoidal elastic bodies. *Tribology International*, Vol.30, pp.599-603.

Peric, D.; Owen, R.J. (1992): Computational model for 3-D contact problems with friction based on the penalty method. *Int.J. for Num. Method. Eng.*, Vol.35, pp.1289-1309.

Simo, J.C.; Hughes, T.J.R. (1997): *Computational inelasticity*, Springer.

Uesugi, M.; Kishida, H. (1986): Influential factors of friction between steel and dry sands. *Soils and Foundations*, Vol.26(2), pp.33-46.

Wriggers, P. (2003): *Computational contact mechanics*, J. Wiley, Chichester.

Wiggers, P.; Vu Van T.; Stein, E. (1990): Finite element formulation of large deformation impact-contact problems with friction. *Computers and Structures*, Vol. 37, pp.319-331.

